

# COLLISIONLESS ELECTRON-ION SHOCKS IN RELATIVISTIC UNMAGNETIZED JET-AMBIENT INTERACTIONS: NON-THERMAL ELECTRON INJECTION BY DOUBLE LAYER

KAZEM ARDANEH<sup>1</sup> AND DONGSHENG CAI

Department of Computer Science, University of Tsukuba, Tenoudai 1-1-1, Tsukuba science city, Ibaraki 305-8573, Japan

KEN-ICHI NISHIKAWA

Department of Physics, University of Alabama in Huntsville, ZP12, Huntsville, AL 35805, USA

<sup>1</sup>kazem.ardaneh@gmail.com

## Abstract

The course of non-thermal electron ejection in relativistic unmagnetized electron-ion shocks is investigated by performing self-consistent particle-in-cell simulations. The shocks are excited through the injection of relativistic jet into ambient plasma, leading to two distinct shocks (named as the trailing shock and leading shock) and a contact discontinuity. The Weibel-like instabilities heat the electrons up to approximately half of ion kinetic energy. The double layers formed in the trailing and leading edges then accelerated the electrons by the ion kinetic energy. The electron distribution function in the leading edge shows a clear non-thermal power-law tail which contains  $\sim 1\%$  of electrons and  $\sim 8\%$  of electron energy. Its power-law index is  $-2.6$ . The acceleration efficiency is  $\sim 23\%$  by number and  $\sim 50\%$  by energy and the power-law index is  $-1.8$  for electron distribution function in the trailing edge. The effect of the dimensionality is examined by comparing results of 3D simulation with 2D ones. It exhibits that the electron acceleration is more efficient in 2D.

*Keywords:* acceleration of particles — galaxies: jets — cosmic rays — plasmas — shock waves

## 1. INTRODUCTION

Tightly collimated streams of plasma with speeds close to the speed of light, commonly referred to as relativistic jets, are present in a variety of astrophysical objects, e.g., pulsar wind nebulae (PWNe) powered by the relativistic wind of pulsars, gamma-ray bursts (GRBs) from the death of massive stars or compact star mergers, and active galactic nuclei (AGNs) at the center of galaxies. The relativistic jets propagate through the ambient medium and excite the double shock structures afterwards. Acceleration of particles is ubiquitous in the astrophysical shocks (Koyama et al. 1995; Eriksen et al. 2011; Masters et al. 2013). Non-thermal emission from these environments is usually considered as synchrotron or inverse Compton radiation from a power-law distribution of electrons accelerated at shock sides (Tautz & Lerche 2012). Due to the lack of a perfectly self-consistent theory of particle acceleration in relativistic shocks, the power-law index and the acceleration efficiency, i.e., the fraction of particles and energy in the non-thermal tail, are usually compared with the observations.

Charged particles may be accelerated via first-order

Fermi acceleration (or diffusive shock acceleration, DSA) in the collisionless shocks. In DSA, particles diffuse back and forth across the shock front and gain energy by scattering from the magnetohydrodynamics waves (Blandford & Ostriker 1978; Bell 1978; Drury 1983; Blandford & Eichler 1987; Bell 2013). However, DSA needs a seed population of particles with energies well in excess of the thermal ones, because only these particles are capable for multiple crossing the shock front and effective scattering by magnetic turbulences. However, it is not apparent how the electrons can reach the threshold energy of DSA. It demands their kinetic energies be comparable to those of the ions. This is known as the electron injection problem (Balogh & Treumann 2013).

In the case of magnetized upstream, the injection of electrons is thought to be directly associated with the background motional electric field  $\mathbf{E}_0 = -\beta_0 \times \mathbf{B}_0$ . They may gain energy from the motional electric field while they gyrate-surf around the shock front. Based on the barrier that reflects the electrons toward the upstream, thus capable them for repeatedly energizations, this process is known with distinct names. If the

reflecting barrier has a magnetic source, e.g., gradient of the magnetic field at the leading edge of the shock, the acceleration mechanism is named shock drift acceleration or SDA (Chen & Armstrong 1975; Webb et al. 1983; Begelman & Kirk 1990; Park et al. 2012, 2013; Guo et al. 2014). If the barrier has an electrostatic source, e.g., the electrostatic solitary waves appeared at the leading edge of the shock by Buneman instability (Buneman 1958), the process is called shock surfing acceleration or SSA (Lee et al. 1996; Hoshino & Shimada 2002; Shapiro & Ücer 2003; Amano & Hoshino 2009; Matsumoto et al. 2012). Basically, the SSA process acts only in the electron-ion shocks, because electrostatic barrier would not be generated if the species have the same inertia. Magnetization parameter, obliquity angle of the upstream magnetic field with respect to the shock direction of propagation, and bulk Lorentz factor of the incoming stream may also play significant role in determining the responsible process for particle acceleration.

An interesting question is: “how does the electron ejection operate in unmagnetized electron-ion shocks?”. Due to the lack of upstream motional electric field, we expect a process other than SDA and SSA. Particle-in-cell (PIC) simulations provide a self-consistent description of particle acceleration in collisionless shocks. Our works have been allocated to the large scale PIC simulations of electron injection in unmagnetized relativistic electron-ion shocks. In PIC simulations, the shock waves are usually excited by the so-called injection approach (Hoshino 2001; Hoshino & Shimada 2002; Spitkovsky 2008a,b; Amano & Hoshino 2009; Martins et al. 2009; Sironi & Spitkovsky 2011; Sironi et al. 2013; Guo et al. 2014). Using this approach, a high-speed plasma stream is launched from one end of the computational grid and reflected from a rigid boundary at the opposite end. Subsequently, a shock is excited due to the interactions between the incoming and the reflected streams. Although this method reduces by one-half the number of calculations, it has some disadvantages as well. In this method, the reverse and forward shock are degenerated (not distinguishable) and the simulations are limited to two identical counter-streaming beams. However, we are interested in asymmetric jet-ambient interaction, i.e., the interaction of plasmas with different properties that results in two different shocks, trailing shock (TS) and leading shock (LS), and a contact discontinuity (CD).

In the present work, we have performed a 3D PIC simulation where collisionless double shock is created by an unmagnetized relativistic jet propagating into an unmagnetized ambient plasma. In contrast to the injection method, our asymmetric jet-ambient model is more realistic since it avoids an infinitely sharp CD and permits us to appropriately explore the dynamics of the TS and LS for different jet-ambient pa-

rameters. Beam-plasma (or jet-ambient) systems are susceptible to several instabilities, e.g., electrostatic two-stream or Buneman modes (Buneman 1958), and electromagnetic filamentation (Fried 1959) or Weibel (Weibel 1959) modes. Therefore, the unstable spectrum is not less than 2D. Which of these modes will dominate highly relies on the system parameters (Bret 2009). This undoubtedly clears a demand for studies using a method like ours (Nishikawa et al. 2003, 2005, 2009, 2016; Ardaneh et al. 2014, 2015; Choi et al. 2014), or using asymmetric counter-streaming beams (Niemić et al. 2012; Wieland et al. 2016), cause the most unstable modes excited in various setups can generate the totally different shock waves.

Our paper is dedicated to answer five questions: First, how does the double shock structure form in the unmagnetized jet-ambient interactions? Second, the shocks are characterized by magnetic or electrostatic forces? Third, what are the main processes responsible for electron injection? Forth, what is the resulting electron distribution function? Fifth, what is the effect of the dimensionality?

The simulation model and parameters setup are described in Section 2. The results of the simulations are presented in Section 3. We conclude with a summary in Section 4.

## 2. SIMULATION MODEL AND PARAMETERS SETUP

In our works, an unmagnetized particles jet is injected into an unmagnetized ambient plasma (Nishikawa et al. 2003, 2005, 2009, 2016; Ardaneh et al. 2014, 2015; Choi et al. 2014). Finally, a double shock structure is formed resemble what is schematically illustrated in Figure 1. Deceleration of the jet stream by the magnetic fluctuations (excited in the beam-plasma interactions) results in a CD and two shock waves that divide the jet and ambient plasmas into four regions: (1) unshocked ambient, (2) shocked ambient, (3) shocked jet, and (4) unshocked jet. Henceforward, subscripts 1, 2, 3, and 4 direct to the unshocked ambient, shocked ambient, shocked jet, and unshocked jet, respectively. Quantities with a single index  $\varrho_i$  indicate the value of quantities  $\varrho$  in region  $i$  in rest frame  $i$  and quantities with double indices  $\varrho_{ij}$  show the value of quantities  $\varrho$  in region  $i$  as seen in rest frame  $j$ .

The code employed in the present work is an adopted version of the relativistic electromagnetic particle code TRISTAN (Buneman 1993) with MPI-based parallelization (Niemić et al. 2008). A series of test simulations are already performed to establish a numerical model which best conserves energy and minimizes numerical self-heating. In the PIC simulations including a cold relativistic plasma beam, a numerical heating instabil-

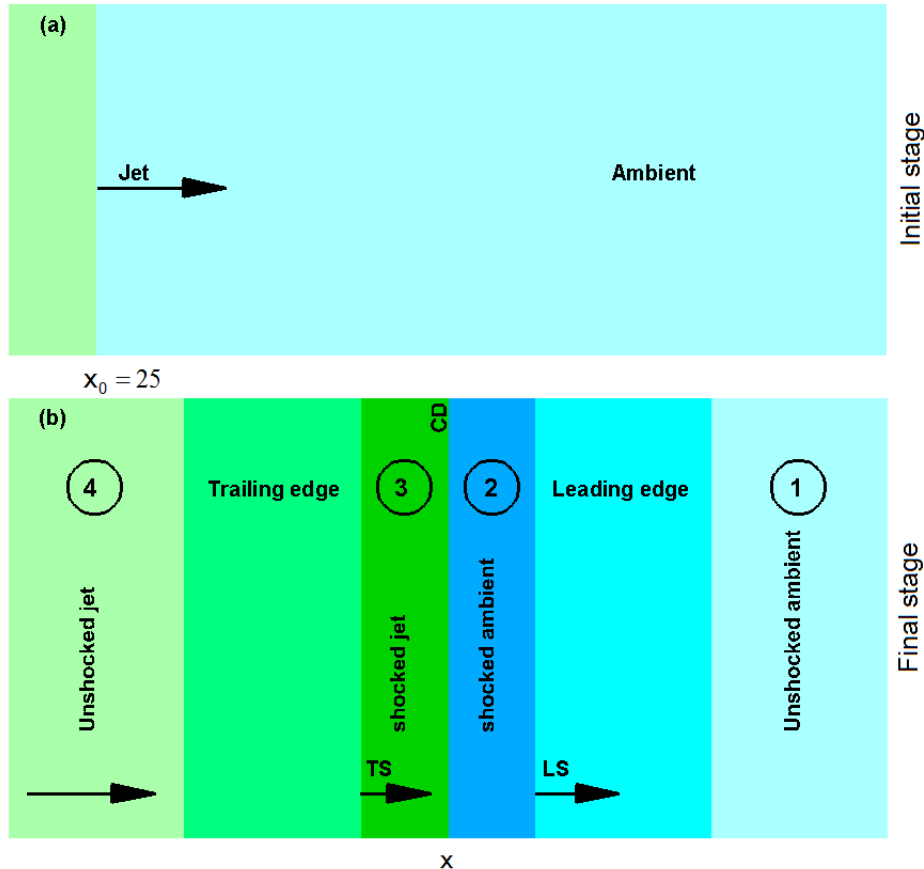


**Figure 1.** An illustration of the jet-ambient interaction showing (a) a particles jet injecting into an ambient plasma and (b) the resulting double shock structure. Naming the shocks is according to Nishikawa et al. (2009).

ity arises when the beam propagates large distances over the numerical grid. The instability is a combination of grid-Cherenkov instability and spurious plasma oscillations (Dieckmann et al. 2006). The latter oscillations are usually excited by coupling between a sideband of the beam mode with the electromagnetic mode. The beam mode has a physical phase speed  $\omega/k = v_b$ , where  $v_b$  is the beam velocity. The beam interaction with the numerical grid, probably through a finite grid instability (Birdsall & Langdon 1991), excites artificial sidebands that are separated from the beam mode by the frequency modulus  $\Delta\omega = 2\pi v_b/\Delta$ , where  $2\pi v_b/\Delta$  is the grid crossing frequency. One of these sidebands may couple to the electromagnetic mode and results in the artificial obliquely propagating waves that are observed in the PIC simulations (Dieckmann et al. 2006). The growth rate of these waves can be reduced by using a higher-order numerical scheme (Yee 1966; Dieckmann et al. 2006). Here, the numerical instability is diminished by means of the fourth-order solver for Maxwell’s curl equations and a weak Friedman filter as presented in Greenwood et al. (2004).

The simulation is performed using a computational grid with  $(\ell_x, \ell_y, \ell_z) = (8005, 245, 245)$ , grid size:  $\Delta x = \Delta y = \Delta z = 1$ . There are six particles per cell per species for the ambient plasma ( $\simeq$  three billions particles per species). The density ratio between the jet and the ambient is 5/3. The simulation frame of reference is the ambient, in which the jet plasma moves to the right in positive  $x$ -direction with bulk speed  $\beta_{41} = 0.995$  (bulk Lorentz factor  $\Gamma_{41} = 10$ ). The jet fills the whole computational box in the  $yz$ -plane and is injected continuously at  $x_0 = 25$ . The jet plasma is injected with energy distribution in the jet rest frame given by a 3D Maxwell-Jüttner distribution  $f(\gamma_4) \propto \gamma_4^2 \beta_4 \exp(-\gamma_4/\theta_4)$  and thermal spread  $\theta_4 = (K_B T_e/m_e c^2)_4 = 0.092$  (relativistically hot,  $\beta_{th4} = 0.4$ ). In the ambient medium, the electrons have a thermal spread  $\theta_1 = (K_B T_e/m_e c^2)_1 = 12.5 \times 10^{-4}$ . In both plasmas, the ions are in thermal equilibrium with the electrons. The  $m_i/m_e$  mass ratio used is 16. The system is numerically resolved with five grid cells per electron skin depth,  $\lambda_{ce} = 5$ , and  $\Delta t = 0.01\omega_{pe}^{-1}$ , where  $\Delta t$  and  $\omega_{pe}$  are the time step and the electron plasma frequency, respectively. The sur-

faces at  $x_{\min}$  and  $x_{\max}$  are rigid reflecting boundaries for the ambient particles, while they are open boundaries for the jet particles. These surfaces are radiating boundaries for the fields based on Lindman’s method (Lindman 1975). Periodic boundary conditions are applied at all other boundaries for both particles and fields. Hereafter, time is normalized to  $\omega_{pe}^{-1}$ , space to the  $\lambda_{ce}$ , particle momentum for species  $s$  to the corresponding  $m_s c$  (e: electron and i: ion), and density to the unshocked ambient density,  $n_1$ . Furthermore, the position  $x$  is measured from  $x_0$ .

For the described setup, according to the hydrodynamic jump conditions for jet-ambient interactions (Zhang & Kobayashi 2005; Nishikawa et al. 2009; Ardaneh et al. 2015), the theoretical predictions for the LS and TS parameters under the adiabatic index  $\tilde{\Gamma} = 4/3$  are summarized in Table 1.

### 3. SIMULATION RESULTS

The jet-ambient interactions include growth of the oblique instability (Bret et al. 2010), and the generation of magnetic fields which decelerate the jet stream and consequently form a double shock structure. At late times the particles are effectively heated, and accelerated. This section aims to explain the scenario in more detail.

#### 3.1. Formation of the CD

When the particles jet interacts with the ambient plasma, the distribution of particles is extremely anisotropic and is susceptible to several instabilities, e.g., electrostatic modes (two-stream or Buneman instabilities), and electromagnetic modes (filamentation or Weibel instabilities). Depending on the jet-to-ambient density ratio, jet and ambient temperatures, and jet drift velocity, two-stream, filamentation, or oblique modes will dominate the linear phase. Whereas perturbations parallel and normal to the jet stream are potentially present, the instability propagates obliquely.

The jet electrons are rapidly decelerated when interact with ambient particles to form electron current filaments in both jet and ambient plasmas (Figure 2a). As a result, the density of the jet electron increases from  $n_{41}/n_1 = 1.7$  to  $n_{41}/n_1 \simeq 2.2$  just behind the jet front (Figure 2b). On other hand, ambient electrons become swept by the incoming jet stream (Figure 2c) and the density of the ambient electron is increased by a factor of three near the jet front (Figure 2d). In this stage (about  $t = 40\omega_{pe}^{-1}$ ), a CD is formed around  $x = 36\lambda_{ce}$  that separate decelerated jet electrons pile from the accelerated ambient electrons pile. The decelerated jet electrons become mainly confined to the left side of CD and pile up in this region. However, due to the CD formation, the accelerated ambient electrons are dominantly confined

to the right side of the CD and they pile up due to the continuous sweeping by the jet inflow. Once trapped in the left side of CD, the jet electron populations commence heating.

Due to ion larger inertia, the jet ions are able to penetrate deeper into the ambient plasma without significant deceleration (Figures 2e and 2f) and ambient ions are present in deeper length of the jet stream (Figures 2g and 2h). Therefore, a certain fraction of both ion populations (jet and ambient) is present in each other before the CD be fully formed. These fractions form a separate population on the two sides of the CD. Each of this population is affected by another plasma medium (jet or ambient) and is reflected back towards the CD. For the ambient fraction, since the ions have no means to either pass through the CD or escape from the continuous flow of jet particles, they are trapped in the left side of CD and will eventually become part of the TS population. This population is visible in the ambient ion phase-space and density plots in Figures 2g and 2h. Due to their highly relativistic forward momentum ( $p_{xi} = 80\text{MeV}/c$ ), deceleration of the jet ions by the ambient plasma will take place in later stages, after the formation of LS in the ambient particles. Therefore, the thermodynamic properties of jet and ambient plasmas (density and temperature) would be different across the LS. It leads to the formation of a double layer (will be discussed in Section 3.4) which causes tapping another fraction of the ambient ions in the right side of the CD. This population will become part of the LS.

#### 3.2. Evolution of the TS

The continuous stream of particles jet and the inability of the particles to cross the CD result in the formation of shocks on both sides of it. Since the ambient plasma located in the right side of our simulation box represents the interstellar medium and the jet plasma coming from the left represents the ejecta, we designate the right shock as the LS and the left shock as the TS. The time evolution of the TS structure is illustrated in Figures 3 as a sequence of snapshots that show the magnetic field component  $B_y$  and the averaged total ion density from  $t = 40\omega_{pe}^{-1}$  (Figure 3a) up to  $t = 280\omega_{pe}^{-1}$  (Figure 3g) with an interval of  $\Delta t = 40\omega_{pe}^{-1}$ . They show that the TS propagate in the positive  $x$ -direction with  $\beta_{ts1} = 0.66$ . The peak value of the total ion density corresponding to the TS reaches  $n_{31}/n_{41} = 2.9$  at  $t = 280\omega_{pe}^{-1}$  (Figure 3g), in well agreement with the hydrodynamic jump conditions for a relativistic gas which predict  $\beta_{ts1} = 0.68$  and  $n_{31}/n_{41} = 2.8$  for the TS in the ambient rest frame (see Table 1).

As shown before in Figure 2g, prior to the full formation of the CD, a fraction of ambient ions is present in a deeper length through the jet stream due to their

**Table 1.** Parameters of the formed double shock structure.

Parameters of the LS		
Parameter	In region (1)	In region (2)
$\gamma_{ls}$	$\gamma_{ls1} = 1.91$	$\gamma_{ls2} = 1.01$
$\beta_{ls}$	$\beta_{ls1} = 0.85$	$\beta_{ls2} = 0.17$
$n_2/n_1$	$n_{21}/n_1 = 16.0$	$n_2/n_{12} = 5.8$
Parameters of the TS		
Parameter	In region (1)	In region (3)
$\gamma_{ts}$	$\gamma_{ts1} = 1.38$	$\gamma_{ts3} = 1.03$
$\beta_{ts}$	$\beta_{ts1} = 0.68$	$\beta_{ts3} = 0.25$
$n_3/n_4$	$n_{31}/n_{41} = 2.8$	$n_3/n_{43} = 4.9$

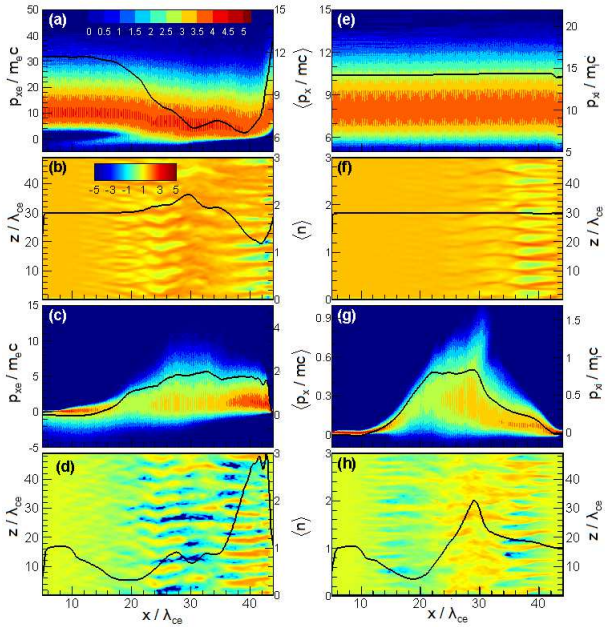


**Figure 2.** Structure of the jet-ambient interaction at time  $t = 40\omega_{pe}^{-1}$  when the fastest jet ions reach  $x = 45\lambda_{ce}$ . The longitudinal phase-space distribution and density in log scale are displayed for: jet electrons in panels (a) and (b), ambient electrons in panels (c) and (d), jet ions in panels (e) and (f), and ambient ions in panels (g) and (h). Over-plotted line in panel (a), (c), (e), and (g), shows the average momentum in  $x$ -direction. Over-plotted line in panel (b), (d), (f), and (h), shows the transversely averaged (in  $yz$ -plane) density normalized to the density in the unshocked ambient. In panels (a), (c), (e), and (g), the phase-space distributions are expressed in  $\log[N(x, p_x)]$ .

higher inertia against sweeping by particles jet. They are continuously pushed towards the CD by the incoming jet stream (see Figures 4). Encountering with the CD, these ambient ions are reflected back into the left side of the CD. Therefore, the reflected ambient ions are trapped and start to pile up in the left side of the CD. This process results in the formation of the ambient ions pile in the TS structure.

The electron contribution in the TS structure belongs

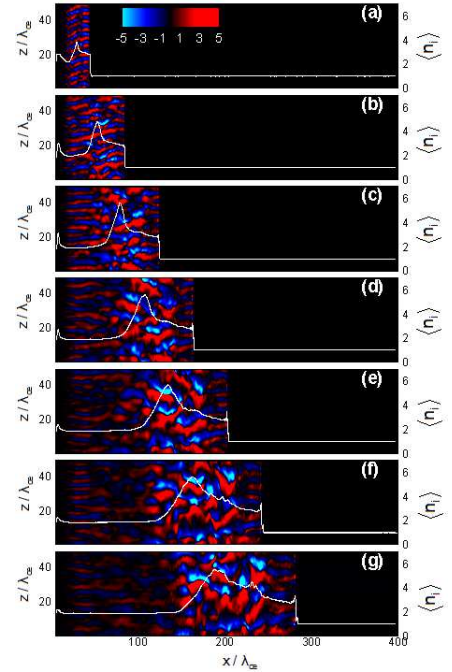


**Figure 3.** The time evolution of the TS structure. Sequence snapshots of the magnetic field component  $B_y$  at  $y = 24\lambda_{ce}$  from  $t = 40\omega_{pe}^{-1}$ , panel (a), up to  $t = 280\omega_{pe}^{-1}$ , panel (g), with an interval of  $\Delta t = 40\omega_{pe}^{-1}$ . Over-plotted in each panel shows the transversely averaged total ion density normalized to the density in the unshocked ambient.

to the jet electrons (see Figures 2a and 2b). The induced magnetic fields due to the Weibel-like instabilities in the jet-ambient collision region resist against propagating of incoming jet electrons into the ambient plasma which cause deceleration of jet electrons and formation of the CD (Figures 5). The formed CD allows no more jet electrons to pass into the ambient medium. They are effectively stopped at the left side of CD and start to pile up as a part of the TS structure.

At  $t = 280\omega_{pe}^{-1}$ , the compression ratio for the TS reaches the level of  $n_{31}/n_{41} = 2.9$  (see Figure 3g) pre-

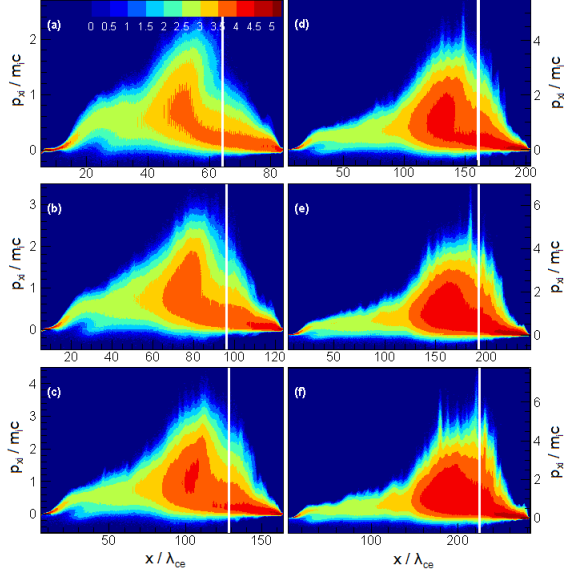


**Figure 4.** The longitudinal phase-space distribution of ambient ions expressed in  $\log[N(x, p_x)]$  during evolution of the TS structure from  $t = 80\omega_{pe}^{-1}$ , panel (a), up to  $t = 280\omega_{pe}^{-1}$ , panel (f), with an interval of  $\Delta t = 40\omega_{pe}^{-1}$ . The position of the CD at each time is shown by a vertical white line.

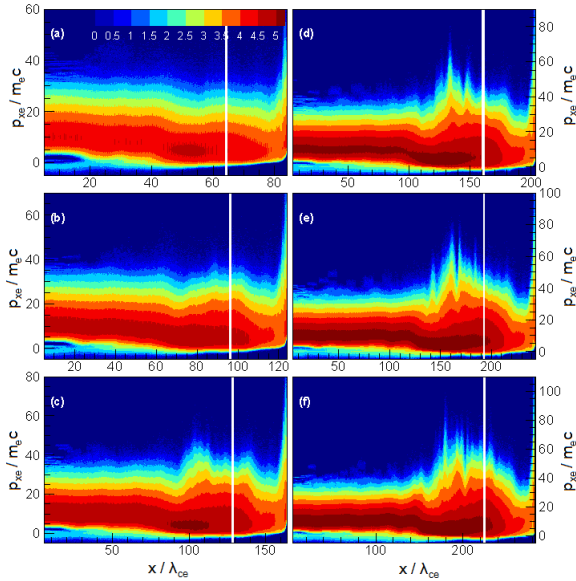


**Figure 5.** The longitudinal phase-space distribution of jet electrons expressed in  $\log[N(x, p_x)]$  during evolution of the TS structure from  $t = 80\omega_{pe}^{-1}$ , panel (a), up to  $t = 280\omega_{pe}^{-1}$ , panel (f), with an interval of  $\Delta t = 40\omega_{pe}^{-1}$ . The position of the CD at each time is shown by a vertical white line.

dicted by the hydrodynamic jump conditions for a 3D relativistic plasma with adiabatic index  $\tilde{\Gamma} = 4/3$ . The compression of electrons is provided solely by the jet electron component (Figures 6a and 6c), while the ion

contribution is supplied by the ambient ions (Figures 6b and 6d). The extended region between the unshocked and shocked jet constitutes the trailing edge. The structure of the trailing edge is exclusively controlled by the strongly nonlinear jet-ambient interactions which result in the formation and merger of current filaments due to the Weibel-like instabilities (Bret et al. 2010). In the vicinity of the TS, the corresponding electromagnetic fields are predominantly transverse. The transverse electric and magnetic fields are related to each other via  $\mathbf{E} = -\boldsymbol{\beta} \times \mathbf{B}$  where  $\boldsymbol{\beta}$  is the velocity of the carriers. The carriers move roughly at the speed of light in the  $x$ -direction (drift velocity  $v_d = E/B \simeq c$ ), hence  $\beta \simeq \beta_x \simeq 1$ . As the results, the transverse fields are as  $E_y = B_z$ , and  $E_z = -B_y$  (see Figures 7). These electric fields cause heating of the particles in transverse directions. Ahead of the filaments (toward the unshocked jet), the electrons of the ambient plasma are absent (Figure 6c). However, a population of hot jet electrons which has been reflected in the CD region streams with slightly relativistic velocity against the incoming jet (see Figures 5). This process excites a Weibel-like two-stream instability (Medvedev & Loeb 1999; Frederiksen et al. 2004; Hededal et al. 2004) between the reflected jet electrons and incoming jet electrons that construct a longitudinal electrostatic perturbations as  $E_x$  (Figure 7g) and associated density modulations, further to the filamentation of the trailing edge (see Figures 7). The amplitude of Weibel-like two-stream perturbations saturates at small level, and their major effect is to heat up the jet electrons in the trailing edge. Toward the TS, the longitudinal electrostatic perturbations become amplified through the stream of the reflected ambient ions in the CD region (see Figures 4), and the fluctuations in  $E_x$  are enhanced (Figure 7g). The longitudinal structures coexist with transverse filaments, indicating that the Weibel-like instability and the density modulation operate in parallel and propagate obliquely.

### 3.3. Evolution of the LS

The evolution of the LS structure is displayed in Figures 8 where the magnetic field component  $B_y$  and the averaged total ion density are shown in sequent snapshots from  $t = 300\omega_{pe}^{-1}$  (Figure 8a) up to  $t = 500\omega_{pe}^{-1}$  (Figure 8f) with an interval of  $\Delta t = 40\omega_{pe}^{-1}$ . As one can see, a density compression appears primarily in the ambient plasma at late stages ( $t \simeq 300\omega_{pe}^{-1}$ ) that we designate as the LS. The compression ratio rises with time until reaches  $n_{21}/n_1 = 6.5$  at the end of the simulation  $t = 500\omega_{pe}^{-1}$  (Figure 8f). The LS structure moves with a speed  $\beta_{ls1} = 0.89$  in the positive  $x$ -direction. In the formed double shock structure, the CD moves in the positive  $x$ -direction with a speed  $\beta_{cd1} = 0.80$ . The hydrodynamic jump conditions for the LS predict

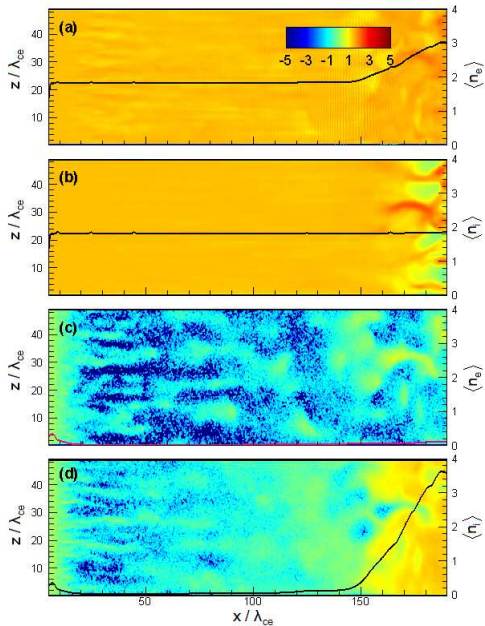


**Figure 6.** Structure of the trailing edge at time  $t = 280\omega_{pe}^{-1}$ . The density of the particle in log scale with an over-plotted line for the average density of the particle normalized to the density in the unshocked ambient is shown for the: (a) jet electron, (b) jet ion, (c) ambient electron, and (d) ambient ion, respectively.

$\beta_{ls1} = 0.85$  and  $n_{21}/n_1 = 16$  in the ambient rest frame (Table 1). Hence, the density jump for the shocked ambient is about a factor of  $\sim 2.5$  smaller than theoretically predicted for a fully developed LS.

The ambient particles (both electrons and ions) are swept by the incoming jet stream. Due to the CD formation in early stages and reflection by the CD, the ambient electrons are mainly trapped in the right side of the CD (Figures 9) and create a compressed region as part of the LS structure. In regards to the ambient ions, as discussed in Section 3.2, they are also present in deeper length of the trailing edge due to their higher rigidity against the incoming jet stream. On other hand, the formed CD and continuous sweeping by jet stream accumulate part of the ambient ions at the right side of the CD (Figures 10). This population contributes in the LS structure. Furthermore, during evolution of the LS, reflection of the ambient ions against the incoming jet happen which these hot counter-streaming ions can be clearly seen as a population with negative momenta in Figures 10. Counter-streaming ions play important role regarding the double layer preservation in the trailing edge which will be discussed in Section 3.4.

By the time the simulation ends, the compression ratio for the TS has not yet reached the compression ratio of a fully developed hydrodynamic shock. The compression of electrons is supplied dominantly by the ambient elec-

trons (Figures 11a and 11c), although the deeply penetrated jet electrons that are trapped in the right side of the CD (see Figure 11a beyond  $x = 420\lambda_{ce}$ ) slightly contribute in the LS structure. The ion contribution is exclusively provided by the ambient ions (Figures 11b and 11d). The extended region between the unshocked and shocked ambient represents the leading edge.

The structure of the electromagnetic fields in the leading edge is mainly controlled by the relativistic ion beam-plasma instabilities, where propagation of dense jet ions into the ambient ions excites the Weibel-like instabilities with wave vectors oriented obliquely to the jet propagation direction (Bret et al. 2010). The Weibel-like instabilities lead to current filamentation (see Figure 11d) and the generation of transverse magnetic fields (Figures 12a, 12b, and 12c). In contrast with the ordinary filamentation instabilities, the electric fields are not purely transverse and there is a finite electrostatic component (see Figures 12d, 12e, 12f and 12g). The relation between the transverse electric and magnetic fields is same as the trailing edge where  $\mathbf{E} = -\boldsymbol{\beta} \times \mathbf{B}$  and hence  $E_y = B_z$ , and  $E_z = -B_y$  (Figures 12). Only when the jet and ambient plasmas are quite symmetric (i.e., same density, temperature, and drift velocity), the filamentation instability would be purely transverse (Bret et al. 2005, 2010). In order not to result in any space charge, the beam and ambient plasmas must pinch absolutely at the same rate. However, this rate highly depends on both the thermal spread (since thermal pressure opposes the magnetic pinching) and the relativistic momentum (and thus the Lorentz factors) of the two populations. Charge imbalance hence appears whenever these parameters are different (see also Choi et al. (2014)). The induced magnetic fields influence the motion of particles. The jet ions are slightly decelerated in bulk and develop a population of slow particles. At the same time the ambient ions, in which filamentation is strongest (Figure 11d), are heated. Thick filaments in the ambient ions are surrounded by electrons. The bulk kinetic energy released by the decelerated jet ions is converted to electron heating in the electric fields that accompany the ion filaments. The volume between the filaments is depleted of ambient ions and occupied by the jet ions. The filamentary structures in the jet electrons are more diffuse on account of their higher temperature (Figure 11a).

### 3.4. Formation of the double layers

As the parallel density structures advect toward the TS, the density of the ambient ion and shock-reflected ambient ions increases (see Figures 10). As a result of shock reflection, a hole in the ambient ion will be appeared within the trailing edge (see  $200\lambda_{ce} \lesssim x \lesssim 260\lambda_{ce}$  in Figure 13h). The hole is filled with the shocked jet

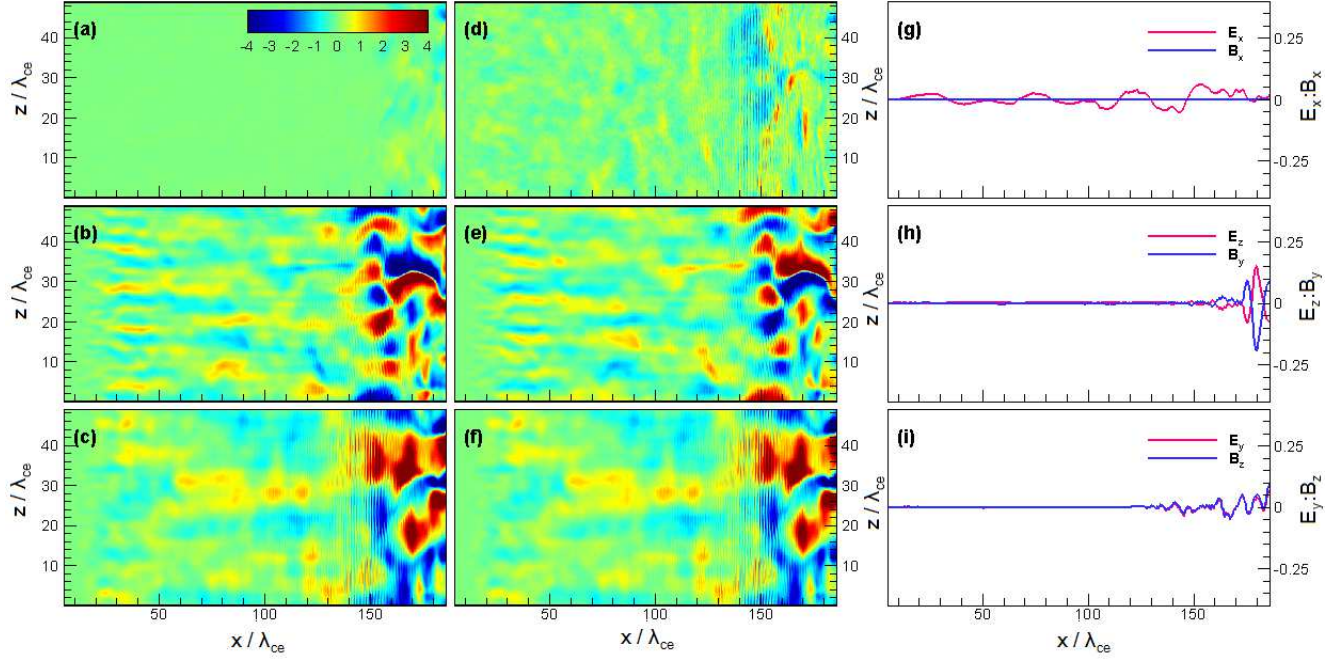


**Figure 7.** Structure of the trailing edge at  $t = 280\omega_{pe}^{-1}$ . Panels (a), (b) and (c) show the components of the magnetic field  $B_x$ ,  $B_y$ , and  $B_z$ , respectively, at  $y = 24\lambda_{ce}$ . Panels (d), (e) and (f) show the components of the electric field  $E_x$ ,  $E_z$ , and  $E_y$ , respectively, at  $y = 24\lambda_{ce}$ . The transversally averaged field components ( $E_x : B_x$ ), ( $E_z : B_y$ ), and ( $E_y : B_z$ ) are shown in panels (g), (h) and (i), respectively.

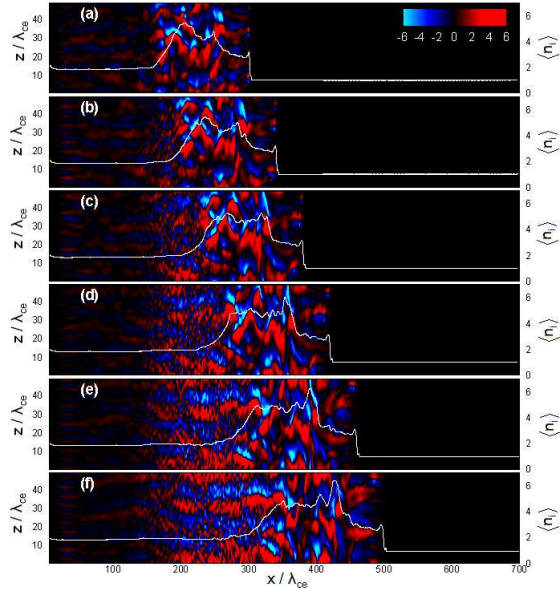


**Figure 8.** The time evolution of the TS structure. Sequence snapshots of the magnetic field component  $B_y$  at  $y = 24\lambda_{ce}$  from  $t = 300\omega_{pe}^{-1}$ , panel (a), up to  $t = 500\omega_{pe}^{-1}$ , panel (f), with an interval of  $\Delta t = 40\omega_{pe}^{-1}$ . Over-plotted in each panel shows the transversally averaged (in  $yz$ -plane) total ion density normalized to the density in the unshocked ambient.

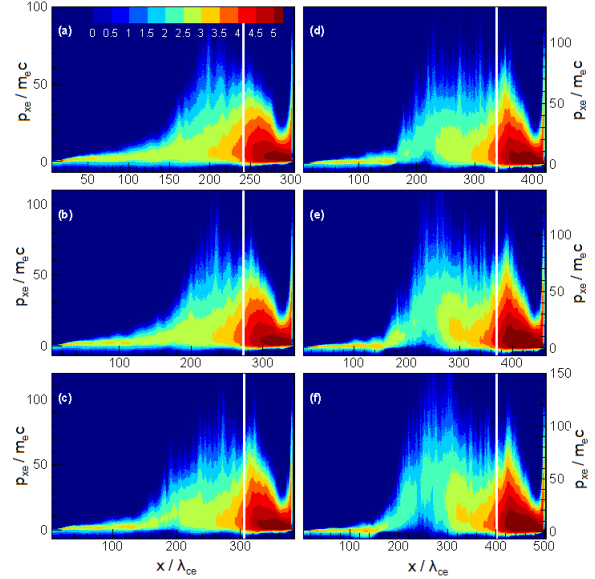


**Figure 9.** The longitudinal phase-space distribution of ambient electrons expressed in  $\log[N(x, p_x)]$  during evolution of the LS structure from  $t = 300\omega_{pe}^{-1}$ , panel (a), up to  $t = 500\omega_{pe}^{-1}$ , panel (f), with an interval of  $\Delta t = 40\omega_{pe}^{-1}$ . The position of the CD at each time is shown by a vertical white line.

electrons, small fraction of the ambient electrons those are trapped in the trailing edge due to the CD, and jet

ions. This process forms a double layer plasma and the associated ambipolar electrostatic field causes trapping



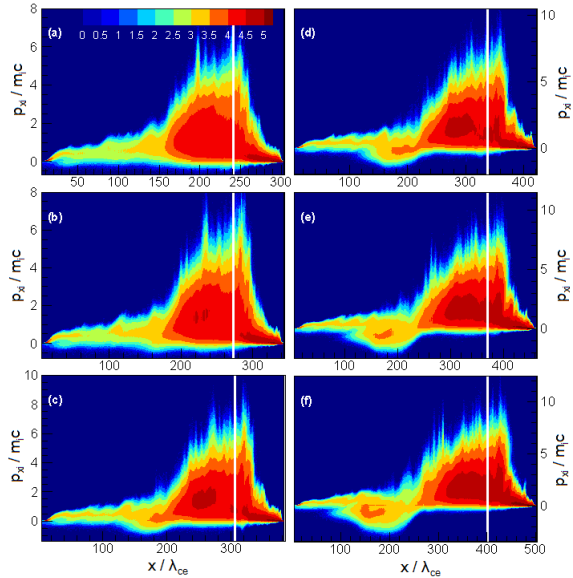


**Figure 10.** The longitudinal phase-space distribution of ambient ions expressed in  $\log[N(x, p_x)]$  during evolution of the LS structure from  $t = 300\omega_{pe}^{-1}$ , panel (a), up to  $t = 500\omega_{pe}^{-1}$ , panel (f), with an interval of  $\Delta t = 40\omega_{pe}^{-1}$ . The position of the CD at each time is shown by a vertical white line.

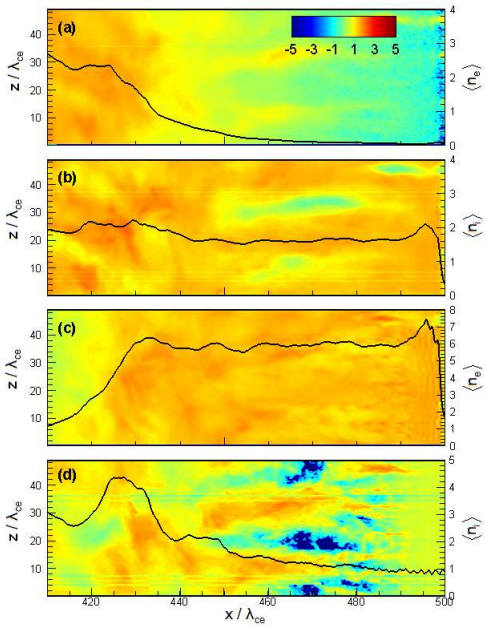


**Figure 11.** Structure of the leading edge at time  $t = 500\omega_{pe}^{-1}$ . The density of the particle in log scale with an over-plotted line for the average density of the particle normalized to the density in the unshocked ambient is shown for the: (a) jet electron, (b) jet ion, (c) ambient electron, and (d) ambient ions, respectively.

of the shock-reflected ambient ions behind the electrostatic field (see  $x \lesssim 200\lambda_{ce}$  in Figure 13h). The electrons are locally accelerated to high energy ( $p_e \simeq 75\text{MeV}/c$  in

Figure 13a) and convect toward the TS region. The accelerated jet electrons and the reflected ambient ions correspond to the freely streaming particle species in a double layer plasma as discussed in Block (1978). Figure 13 presents the structure of the jet-ambient interaction at time  $t = 500\omega_{pe}^{-1}$  that is representative of the characteristics discussed above. The figure shows the longitudinal phase-space distribution of particles, and the density of particle in log scale with an over-plotted which illustrates the average density, for jet electron, ambient electron, jet ion, and ambient ions.

The double layer in the trailing edge accelerates jet electrons out of the bulk to an average momentum  $\langle p_e \rangle \simeq 40\text{MeV}/c$  (see Figure 13a and Figure 15d). The formed double layer is not stationary, it is one with a floating potential instead (Figure 14). Therefore, the energy of the jet electrons increases in time while the jet electron temperature remains unchanged (will be shown in Section 3.5). The energy of the accelerated electrons exceeds their thermal energies, even after the Weibel-like instabilities have heated the electrons (the average  $\langle p_{ye} \rangle \simeq \langle p_{ze} \rangle \simeq 20\text{MeV}/c$ , see Figure 15b). Therefore, the kinetic energy of the jet electrons have been increased through the double layer potential where  $e\langle\phi\rangle \simeq 20\text{MeV}$  (Figure 15c). According to the Bohm criterion (Block 1978), a double layer demands a drift speed that is rather faster than the thermal speed. This criterion is well satisfied whereas  $v_d \simeq c$ . The accelerated jet electrons then interacts with the ambient medium through a oblique Weibel-like instability, which the corresponding electromagnetic fields are responsible for the spikes in the electrons phase-space distribution within the interval  $200\lambda_{ce} \lesssim x \lesssim 300\lambda_{ce}$  in Figures 13a and 13c. A secondary two-stream instability was also found in Newman et al. (2001); Dieckmann & Bret (2009), although the jets (beams) were non-relativistic there. Principally, the type of instability is not important for the evolution of the double layer because it forms behind it. The electric field of the double layer is strong inasmuch as it can slow down the jet ions by a factor of 50 % from the initial momentum  $p_i = 80\text{MeV}/c$  (Figure 13e), which supports the energy for the electron acceleration. The double layer is thus an ion decelerator which is characteristic of an electrostatic shock. The corresponding electrostatic TS involving only the ambient ions occurs at  $x = 340\lambda_{ce}$ .

Another double layer structure exists in the leading edge (see Figure 14) which move with a speed  $\beta \simeq c$ . The density and temperature of the jet and ambient plasmas differ through the leading edge (see Figures 13). Therefore, the quasi-neutrality is violated and a double layer will be formed. This double layer accelerates ambient electrons up to an average energy  $\simeq 5\text{MeV}$  (see Figure 13c and Figure 15c). Similar to the previous one,

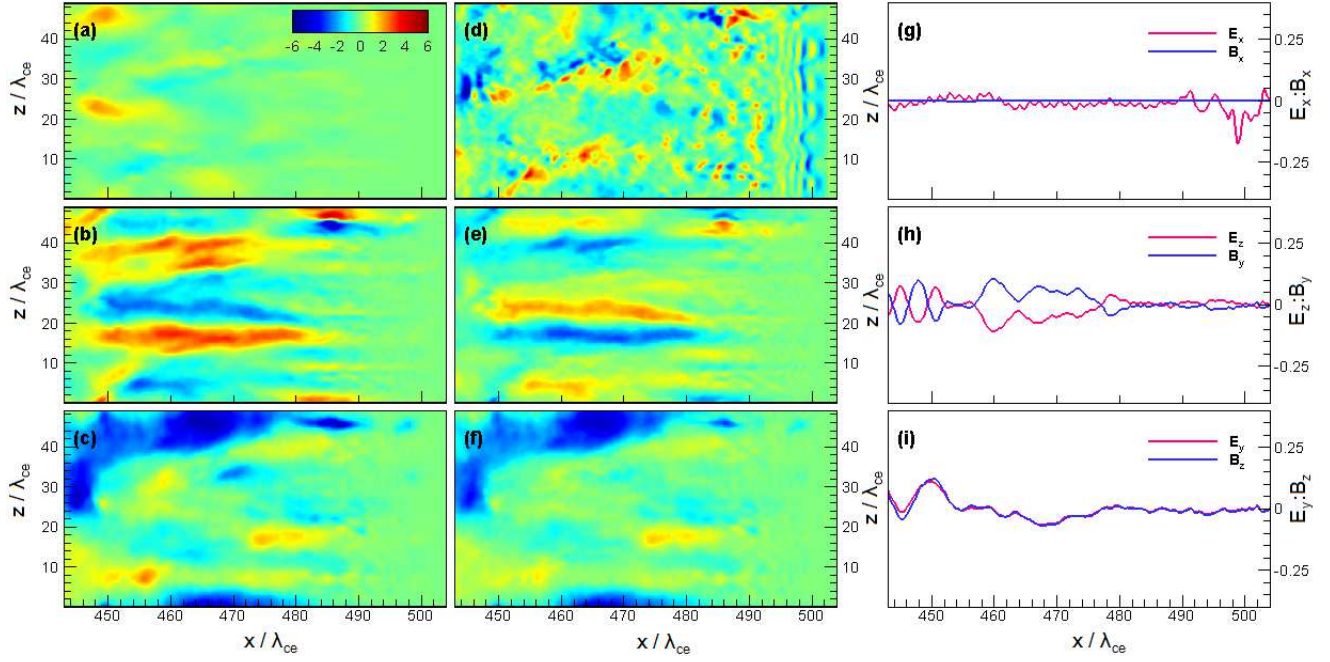


**Figure 12.** Structure of the leading edge at  $t = 500\omega_{pe}^{-1}$ . Panels (a), (b) and (c) show the components of the magnetic field  $B_x$ ,  $B_y$ , and  $B_z$ , respectively, at  $y = 24\lambda_{ce}$ . Panels (d), (e) and (f) show the components of the electric field  $E_x$ ,  $E_z$ , and  $E_y$ , respectively, at  $y = 24\lambda_{ce}$ . The transversally averaged field components ( $E_x : B_x$ ), ( $E_z : B_y$ ), and ( $E_y : B_z$ ) are shown in panels (g), (h) and (i), respectively.

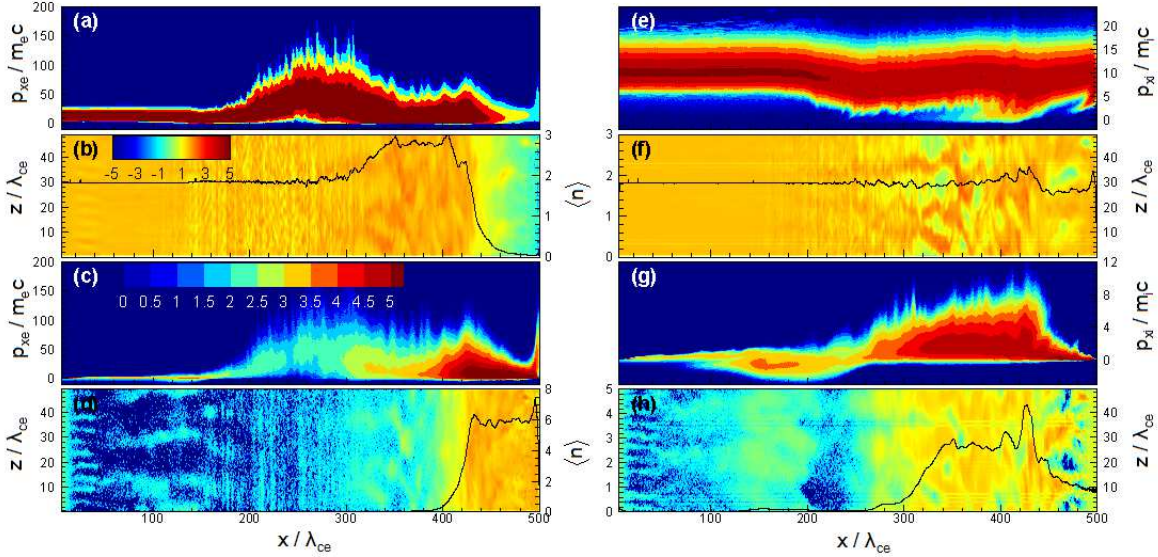


**Figure 13.** Structure of the jet-ambient interaction at time  $t = 500\omega_{pe}^{-1}$  when the fastest jet ions reach  $x = 505\lambda_{ce}$ . The longitudinal phase-space distribution and density in log scale are displayed for: jet electrons in panels (a) and (b), ambient electrons in panels (c) and (d), jet ions in panels (e) and (f), and ambient ions in panels (g) and (h). Over-plotted line in panel (a), (c), (e), and (g), shows the average momentum in  $x$ -direction. Over-plotted line in panel (b), (d), (f), and (h), shows the transversally averaged (in  $yz$ -plane) density normalized to the density in the unshocked ambient. In panels (a), (c), (e), and (g), the phase-space distributions are expressed in  $\log[N(x, p_x)]$ .

the double layer in the leading edge is strong enough to slow down the jet ions stream and supply the energy for electron acceleration. As a result, another electrostatic shock including also the jet ions forms near the jet ions front (see Figures 11b and 11c).

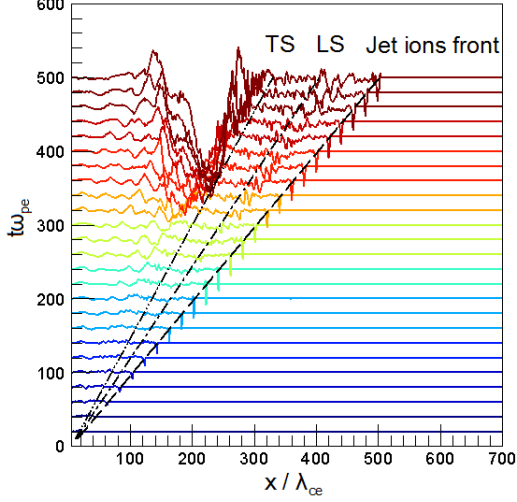


**Figure 14.** The stacked profiles of the transversely averaged  $E_x$  is shown from  $t = 20\omega_{pe}^{-1}$  up to  $500\omega_{pe}^{-1}$  with an interval of  $\Delta t = 20\omega_{pe}^{-1}$ . Dashed-dot-dot, dashed-dot, and dashed lines represent the TS, LS, and jet ions front, respectively.

The transverse electric and magnetic fields ( $E \simeq B$ , and the energy density stored in the magnetic fields reach about 10% of the jet energy density in the shocked region, see Figure 15a) in  $yz$ -plane result in a  $\mathbf{E} \times \mathbf{B}$  drift motion of electrons in  $x$ -direction. During this motion, the electrons become efficiently heated. The maximum attainable energy for an electron during drift motion has been estimated analytically (Medvedev 2006; Ardaneh et al. 2015) where the electron energy density is proportional to the square root of the magnetic field energy density, normalized to the total incoming energy density,  $\epsilon_e \simeq \sqrt{\epsilon_B}$ . Using this expression, the average change in the electron energy,  $\langle \Delta E_e / m_e c^2 \rangle = \langle \Delta \gamma_e \rangle$ , due to the transverse electric fields of ion filaments is displayed in Figure 15b. As one can see, in the trailing edge,  $x \lesssim 340\lambda_{ce}$ , the electrons (mostly jet electrons) are heated by the ion filament up to 20 MeV. Furthermore, due to the presence of a double layer in the trailing edge, the electrons can gain more energy within the double layer electric field. The maximum attainable energy through the double layer in the trailing edge is  $e\langle\phi\rangle \simeq 20\text{MeV}$  (Figure 15c). Hence, ion filaments and double layer together increase the electrons energy in the trailing edge by an average energy of 40 MeV (Figure 15d). A similar process in the leading edge increases the average energy of ambient electrons energy to 5 MeV.

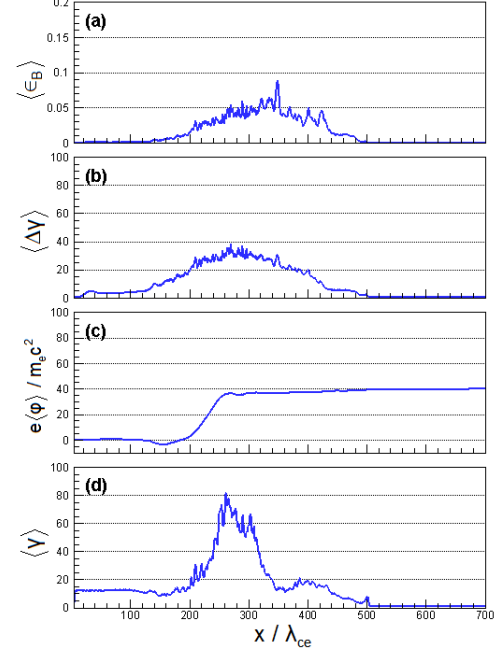


**Figure 15.** Electrons heating and acceleration. Displayed are: (a) magnetic energy density  $\epsilon_B$ , normalized to the jet energy density, (b) average change in the electron energy due to the transverse electric fields of ion filaments,  $\langle \Delta E_e / m_e c^2 \rangle = \langle \Delta \gamma_e \rangle$ , (c) average change in the electron kinetic energy due to the double layer electric field,  $e\langle\phi\rangle / m_e c^2$ , and (d) average electron energy,  $\langle \Delta \gamma_e \rangle$ , along  $x$ -direction. All panels are calculated at  $t = 500\omega_{pe}^{-1}$ .

### 3.5. Evolution of the electron distribution function

The common observational characteristic of PWNe, GRBs afterglows, and AGN jets is a broad non-thermal spectrum of synchrotron and inverse Compton emission that extend from the radio up to the gamma-ray band. One of the key ingredients in creating this non-thermal spectrum is a non-thermal, high-energetic electron population. This population may be seen in the electron distribution function, where a pure 3D Maxwell-Jüttner distribution (in our case) does not account for the high energies. In fact, a more complex distribution function is expected as a result of electron acceleration. Shown in Figures 16 are the evolution of the electron distribution function in time (Figure 16a taken in the leading edge, Figure 16b taken in the shocked region, and Figure 16c taken in the trailing edge). At late stages, in both leading and trailing edges, the electron distribution function consists of a drifting Maxwell-Jüttner distribution (our rest frame of reference is the ambient) and a high-energy tail. The electron distribution function in the shocked region illustrates a hot well mixed population (includes jet and ambient) with a drifting Maxwell-Jüttner distribution. The electron distribution functions in Figures 16a and 16c clearly develop a non-thermal tail

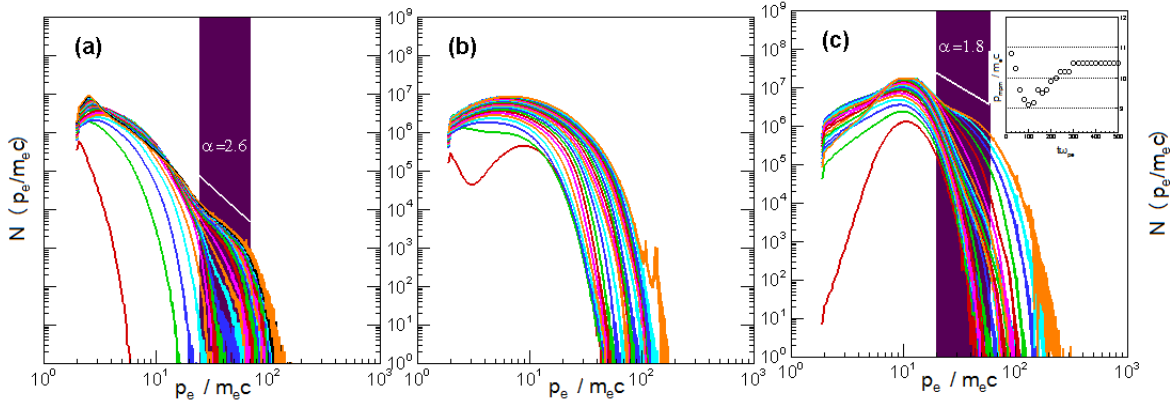


**Figure 16.** Evolution of the electron distribution function from  $t = 20\omega_{pe}^{-1}$  (leftmost red line) up to  $500\omega_{pe}^{-1}$  (rightmost orange line) with an interval of  $\Delta t = 20\omega_{pe}^{-1}$ : (a) for ambient in the leading edge taken at  $(\beta_{41} - \beta_{ts1})t\omega_{pe}^{-1}$ , (b) for ambient+jet in the shocked region taken at  $(\beta_{ts1} - \beta_{ts1})t\omega_{pe}^{-1}$ , and (c) for jet in the trailing edge taken at  $x/\lambda_{ce} \lesssim \beta_{ts1}t\omega_{pe}^{-1}$ . White line in panel (a) and (c) shows a power-law fit to the non-thermal component in the electron distribution function at the latest time. The inset in panel (c) shows the time evolution of the most probable momentum for jet electrons,  $p_{mpm}$ .

over time. For  $t \gtrsim 300\omega_{pe}^{-1}$ , when the counter-streaming shock-reflected ions come to account and strong double layer form in the trailing edge, the electron are accelerated within the double layer. In this manner, their temperature do not changed significantly. This process is visible in the inset panel of Figure 16c where the most probable momentum,  $p_{mpm}$ , is constant for  $t \gtrsim 300\omega_{pe}^{-1}$ . The white line shows a power-law fit to the non-thermal, high-energy electron population. The power-law begins around  $p_{min} = 12.5\text{MeV}/c$  and extends to high energies with an exponential cutoff. The power-law index  $\alpha$ , defined in  $N(p) \propto p^{-\alpha}$ , has a best-fit value  $\alpha = 2.6$  in the leading edge, and  $\alpha = 1.8$  in the trailing edge. The non-thermal tail in the electron distribution function (Figure 16a and 16c) extends with time to higher and higher energies. It clearly demonstrates that electron acceleration is efficient and persevering in time. Regarding electron distribution function in the leading edge, at time  $t = 500\omega_{pe}^{-1}$ , the non-thermal tail for  $p \geq 12.5\text{MeV}/c$  contains  $\sim 1\%$  of electrons ( $\sum_{p_e \geq p_{min}} N_i / \sum N_i$ ) and  $\sim 8\%$  of electron energy ( $\sum_{p_e \geq p_{min}} N_i E_i / \sum N_i E_i$ ) in the leading edge. The acceleration efficiency for electron is  $\sim 23\%$  by number and  $\sim 50\%$  by energy in the trailing edge, calculated in the same way as the leading edge.

Theoretically, an ensemble of electrons with a power-law energy distribution function  $N(\gamma)d\gamma \propto \gamma^{-\alpha}d\gamma$  (for the ultra-relativistic speeds  $\gamma \propto p$ ) result in a radiation spectrum  $F(\nu) = \nu^{-s}$  (Rybicki & Lightman 1979), where the spectral index  $s$  is related to the particle distribution index  $\alpha$  by  $s = (\alpha - 1)/2$ . Therefore,  $\alpha = 1.8 - 2.6$  in the electron energy distribution results in the spectral index  $s = 0.4 - 0.8$  which is in the range of the radio up to optical and X-ray emission (Bietenholz et al. 1997; Panaitescu 2001; Panaitescu & Kumar 2002).

### 3.6. Dependence on the dimensionality

Our reference run is performed on a 3D spatial domain. To examine effect of the dimensionality, we have run a simulation with the same physical parameters as in our reference run, but in 2D computational domain. For the 2D run, the box size along the  $z$ -direction is only  $1.6c/\omega_{pe}$  (8 grid cells). We find that the phase-space distributions of the particles and density structure agree well in terms of both the formed shock structure and the double layers in the trailing and leading edges. However the adiabatic index  $\tilde{\Gamma} = 3/2$  in the 2D domain results in the slower shocks ( $\beta_{ts1} = 0.60$  and  $\beta_{ls1} = 0.87$ ) and smaller particle compression ( $n_{31}/n_{41} = 2.0$  and  $n_{21}/n_1 = 11.63$ ) compared to the 3D structure.

The time evolution of the electron distribution function from the 2D run is displayed in Figures 17. In 2D run, the observed power-law index of the electron distribution function is  $\alpha = 3.2$  in the leading edge, and  $\alpha = 2$  in the trailing edge. The harder spectral index in 2D run can mean that the electron acceleration is more efficient than in 3D. Actually, the non-thermal tail in electron distribution function contains  $\sim 2.3\%$  of electrons and  $\sim 14\%$  of energy in the leading edge, and  $\sim 24.4\%$  of electrons and  $\sim 51.4\%$  of energy in the trailing edge, respectively.

In the early phase, the fields generated in the 3D simulation are stronger than in 2D, due to the additional transverse dimension that the 3D instability can gather particles from. However, at later stages the growth of fields in the 2D simulation surpasses the 3D case (Stockem et al. 2015). This is primarily caused by two effects: First, a 2D system has less degrees of freedom for the motion of particles; they are then more easily trapped and saturate in a larger amplitude. Second, ion

current filaments can merge to larger transverse structures. This also can be followed in the 3D simulation but in longer times for larger box.

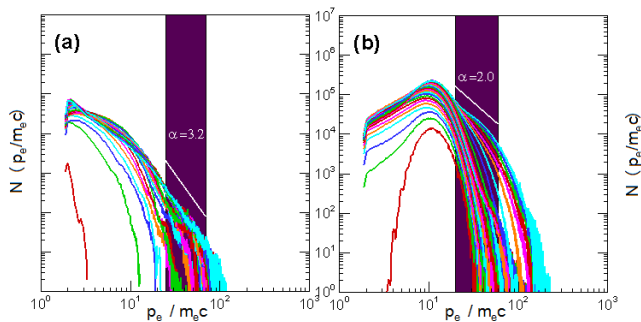


**Figure 17.** 2D run: Evolution of the electron distribution function from  $t = 20\omega_{pe}^{-1}$  (leftmost red line) up to  $560\omega_{pe}^{-1}$  (rightmost cyan line) with an interval of  $\Delta t = 20\omega_{pe}^{-1}$ : (a) for ambient in the leading edge taken at  $(\beta_{41} - \beta_{1s1})t\omega_{pe}^{-1}$ , and (b) for jet in the trailing edge taken at  $x/\lambda_{ce} \lesssim \beta_{ts1}t\omega_{pe}^{-1}$ . White line shows a power-law fit to the non-thermal component in the electron distribution function at the latest time.

#### 4. SUMMARY AND CONCLUSIONS

Our motivation has been to recognize a mechanism that may accelerate electrons in the unmagnetized shock to energies, so that they can experience the DSA to ultra-relativistic energies. The observational radio synchrotron emissions from the supernova remnant shocks confirm the existence of such electrons (Uchiyama et al. 2007; Eriksen et al. 2011) although their origin is still unclear. The electrons are injected into the DSA, if their kinetic energies be comparable to the ion kinetic energies (Hoshino et al. 1992; Hoshino 2001; Amano & Hoshino 2009; Reynolds 2008; Hillas 2005). It is believed that the electrons are pre-accelerated by instabilities, those are excited by ion beams in the transition region of shocks (Cargill & Papadopoulos 1988; Hoshino et al. 1992; Hoshino 2001). The origin of the ion beams is either the reflection of upstream ions by the shock or the leaking of downstream ions into the upstream plasma. However, Buneman instability (Buneman 1958) and Weibel-like two-stream instability invoked in previous works (Hoshino 2001; Hoshino & Shimada 2002; Hededal et al. 2004; Medvedev 2006; Amano & Hoshino 2009) are not strong enough to inject the electrons into the DSA. They may just transfer a few percent of the ions kinetic energy to the electrons.

The present work investigates the secondary processes triggered by the Weibel-like instabilities with a 3D PIC code (Buneman 1993; Niemiec et al. 2008). The employed model of the simulation completely differs from the injection model used in several related papers (Hoshino 2001; Hoshino & Shimada 2002; Spitkovsky

2008a,b; Amano & Hoshino 2009; Martins et al. 2009; Sironi & Spitkovsky 2011; Sironi et al. 2013; Guo et al. 2014). We have modeled an unmagnetized relativistic jet propagating into an ambient plasma. They contain ions and electrons. We have simulated the double shock system and our model is hence self-consistent. The jet moves with bulk speed  $0.995c$  in the  $x$ -direction relative to the ambient plasma. The initial temperatures of species in the jet and ambient have been set to 46.25 keV and 0.6 keV, respectively, in their rest frame.

Three spatial directions have been resolved by the current PIC simulation, which implies that the wave spectrum driven by the Weibel-like instabilities propagate obliquely with respect to the jet propagation direction (Bret et al. 2005; Bret 2009; Bret et al. 2010). Both filamentation and two-stream modes are present and operate simultaneously in electron heating. Consequently, strong fluctuations occur in the density of electrons and ambient ions that result in the formation of the double shock system. The conclusions of the work presented here can be summarized as answers to the remarked questions in Section 1.

1. “How does the double shock structure form in the unmagnetized jet-ambient interactions?”

At early times, a CD forms between the decelerated jet electron and the swept ambient electrons. Consequently, the jet electrons are accumulated at the right side of CD as part of TS. Additionally, a fraction of the ambient ions are located in the right side of CD cause of ion higher rigidity. They are swept by the jet continuous stream and contribute at the TS due to the reflection by the CD. Therefore, we have defined the TS as a pile of jet electrons and a fraction of ambient ions. On the other hand, the swept ambient electrons and the swept ambient ions in the right side of CD construct the LS. In a longer simulation, when the jet ions become significantly decelerated, we expect that jet ions contribute in the both TS and LS structures.

2. “The shocks are characterized by magnetic or electrostatic forces?”

The electrostatic and magnetic effects are strongly activated at the same time in the captured double shock structure (a similar situation was also found for non-relativistic shocks in Matsumoto et al. (2013)). The transverse magnetic fields are induced due to the Weibel-like instabilities in the jet-ambient interaction. These fields are dominantly azimuthal and associated with the ion current filaments. In the shocked region, the magnetic energy density,  $\epsilon_B$ , is near 10% of jet energy density.

Transverse electric fields are also present around the ion current filaments due to the density filamentation by Weibel-like instabilities. The longitudinal electrostatic fields are due to the formed double layers in the trailing and leading edges. Both electrostatic force and  $\mathbf{E} \times \mathbf{B}$  drift motion are important and play significant role in electron dynamics. However, in the shocked region, the induced magnetic fields facilitate energy transfer between the jet and ambient plasma.

3. “What are the main mechanisms responsible for electron injection?”

At first, the electrons are heated up to a maximum energy density  $\epsilon_e \simeq \sqrt{\epsilon_B}$  via  $\mathbf{E} \times \mathbf{B}$  drift motion. Additionally, the shock-reflected ambient ions trigger a double layer in the trailing edge which evolves consequently into an electrostatic shock. A double layer is also formed in the leading edge due to the decelerated jet ions and ambient electrons. The secondary electron energization process is associated with the electric fields of double layers. The drift speed of the free streaming particles is well in excess of the thermal one. It maintains the double layer structures in time. The substantial energy stored in the jet ions causes the electron acceleration up to 75 MeV. The double layers convert forward energy of jet ions into forward energy of electrons, without heating up the electrons. Electrons can thus be accelerated more efficiently by a double layer than by a shock because the latter spends part of flow energy for heating.

4. “What is the resulting electron distribution function?”

The electron distribution function includes a non-thermal tail that contains  $\sim 1\%$  of electrons and  $\sim 8\%$  of electron energy in the leading edge, and  $\sim 23\%$  of electrons and  $\sim 50\%$  of electron energy in the trailing edge, respectively. The power-law fit to the non-thermal tail has index  $\alpha = 1.8$  in the trailing edge,  $\alpha = 2.6$  in the leading edge, respectively. These results confirm that the double layers are more efficient than shocks in electron acceleration. Based on the PIC simulations, the shocks efficiency in particle acceleration is  $\sim 1\%$  by number and  $\sim 10 - 15\%$  by energy (Spitkovsky 2008b; Martins et al. 2009; Sironi & Spitkovsky 2011; Sironi et al. 2013; Guo et al. 2014).

5. “What is the effect of the dimensionality?”

In the performed 2D simulation, the power-law index in the non-thermal tail is  $\alpha = 3.2$  in the lead-

ing edge, and  $\alpha = 2$  in the trailing edge, respectively. The non-thermal tail contains  $\sim 2.3\%$  of electrons and  $\sim 14\%$  of electron energy in the leading edge, and  $\sim 24.4\%$  of electrons and  $\sim 51.4\%$  of electron energy in the trailing edge, respectively. These mean that the electron acceleration in 2D is more efficient than in 3D.

The present work uses a ion-electron mass ratio  $m_i/m_e = 16$ . Although this low mass ratio is necessary to keep the computational costs of 3D simulations reasonable, it changes the growth rate of the unstable modes as well. In the early growth stage, when the ions are not included in the instabilities, the magnetic fields energy increases exponentially, independent of the mass ratio. However, the mass ratio effect becomes significant in the nonlinear phase. When it is small compared to the realistic one (1836), the saturation level of the magnetic field becomes higher, since the ion current filaments merge as similar as the electron ones, due to the mutual attraction between the filaments. Increasing the mass ratio will reduce the ion isotropization rate and the rate of kinetic energy exchange with electrons via the Weibel-like instabilities. Moreover, it is found that Weibel-like modes govern the high beam density regimes in the beam-plasma interactions (Bret & Dieckmann 2010). The domain of these modes expands as the mass ratio decreases. Consequently, the domains governed by the oblique modes shrink with decreasing the mass ratio. Therefore, our low mass ratio gives a higher importance to the Weibel-like instabilities than what they normally have.

Regarding the double layers, the electrostatic potential jumps in the trailing and leading edges are established by the electron density and temperature jumps across the shocks. These jumps are in turn decided by the shock jump conditions that do not change significantly for different ion-to-electron mass ratios. Hence, the electrostatic potentials of the double layers are independent on the mass ratio. However, increasing the mass ratio will increase the kinetic energy of the ions. The ions are thus more difficultly slowed down in the double layers, causing the slower rate of kinetic energy exchange between the ions and electrons. In this manner, the TS, LS, and CD acquire their steady-state velocity later.

We thank Masahiro Hoshino, and Takanobu Amano for valuable discussions. The work of KN is supported by NSF AST-0908010, AST-0908040, NASA-NNG05GK73G, NNX07AJ88G, NNX08AG83G, NNX08AL39G, NNX09AD16G, NNX12AH06G, NNX13AP-21G, and NNX13AP14G grants. The simulations presented here were performed on the KDK

computer system at Research Institute for Sustainable

Humanosphere, Kyoto University.

## REFERENCES

- Amano, T., & Hoshino, M. 2009, *ApJ*, 690, 244
- Ardaneh, K., Cai, D., & Nishikawa, K-I. 2014, *NewA*, 33, 1
- Ardaneh, K., Cai, D., Nishikawa, K-I., & Lembége, B. 2015, *ApJ*, 811, 57
- Balogh, A., & Treumann, R. A., 2013, *Physics of Collisionless Shocks: Space Plasma Shock Waves*, Springer Science & Business Media, New York, First edition
- Begelman, M. C., & Kirk, J. G. 1990, *ApJ*, 353, 66
- Bell, A. R. 1978, *MNRAS*, 182, 147
- Bell, A. R. 2013, *Astroparticle Physics*, 43, 56
- Bietenholz, M. F., Kassim, N., Frail, D. A., Perley, R. A., Erickson, W. C., & Hajian, A. R. 1997, *ApJ*, 490, 291
- Birdsall, C. K., Langdon, A. B., 1991. *Plasma physics via computer simulation*. Institute of Physics Publishing, Bristol
- Blandford, R., & Eichler, D. 1987, *Physics Reports*, 154, 1
- Blandford, R. D., & Ostriker, J. P. 1978, *ApJ*, 221, L29
- Block, L. P., 1978, *Ap&SS*, 55, 59
- Bret, A., Firpo, M.-C., & Deutsch, C. 2005, *PhRvL*, 94, 115002
- Bret, A. 2009, *ApJ*, 699, 990
- Bret, A., Gremillet, L., & Benisti, D. 2010, *PhRvE*, 81, 036402
- Bret, A., & Dieckmann, M. E. 2010. *Physics of Plasmas*, 17, 032109
- Buneman, O. 1958, *PhRvL*, 1, 8
- Buneman, O. 1993, Tristan, in *Computer Space Plasma Physics, Simulation Techniques and Software*, ed. H. Matsumoto & Y. Omura (Tokyo: Terra Scientific Publishing Company), 67
- Cargill, P. J., & Papadopoulos, K. 1988, *ApJ*, 329, L29
- Chen, G., & Armstrong, T. P. 1975, in *Proc. 14th ICRC (Munich)*, Vol. 5, 1814
- Choi, E. J., Min, K., Nishikawa, K.-I., & Choi, C. R. 2014, *Physics of Plasmas*, 21, 072905
- Dieckmann, M. E., & Bret, A. 2009, *ApJ*, 694, 154
- Dieckmann, M. E., Frederiksen, J. T., Bret, A., & Shukla, P. K. 2006, *Physics of Plasmas*, 13, 112110
- Drury, L. O. 1983, *Reports on Progress in Physics*, 46, 973
- Eriksen, K. A., Hughes, J. P., Badenes, C., Fesen, R., Ghavamian, P., Moffett, D., Plucinsky, P. P., Rakowski, C. E., Reynoso, E. M., & Slane, P. 2011, *ApJL*, 728, L28
- Frederiksen, J. T., Hededal, C. B., Haugbølle, T., & Nordlund, Å. 2004, *ApJL*, 608, L13
- Fried, B. D., 1959, *Physics of Fluids*, 2, 337
- Greenwood, A. D., Cartwright, K. L., Luginsland, J. W., & Baca, E. A. 2004, *Journal of Computational Physics*, 201, 665
- Guo, X., Sironi, L., & Narayan, R. 2014, *ApJ*, 794, 153
- Hededal, C. B., Haugbølle, T., Frederiksen, J. T., & Nordlund, Å. 2004, *ApJL*, 617, L107
- Hillas, A. M. 2005, *Journal of physics g: nuclear and particle physics*, 31, R95
- Hoshino, M., Arons, J., Gallant, Y. A., & Langdon, A. B., 1992, *ApJ*, 390, 454
- Hoshino, M. 2001, *Progress of Theoretical Physics Supplements*, 143, 149
- Hoshino, M., & Shimada, N. 2002, *ApJ*, 572, 880
- Koyama, K., Petre, R., Gotthelf, E. V., Hwang, U., Matsuura, M., Ozaki, M., & Holt, S. S. 1995, *Nature*, 378, 255
- Lee, M. A., Shapiro, V. D., & Sagdeev, R. Z. 1996, *Journal of Geophysical Research*, 101, 4777
- Lindman, E. L., 1975, *Journal of Computational Physics*, 18, 66
- Martins, S. F., Fonseca, R. A., Silva, L. O., & Mori, W. B. 2009, *ApJL*, 695, L189
- Masters, A., Stawarz, L., Fujimoto, M., Schwartz, S. J., Sergis, N., Thomsen, M. F., Retino, A., Hasegawa, H., Zieger, B., Lewis, G. R., Coates, A. J., Canu, P., & Dougherty, M. K. 2013, *Nature Physics*, 9, 164
- Matsumoto, Y., Amano, T., & Hoshino, M. 2012, *ApJ*, 755, 109
- Matsumoto, Y., Amano, T., & Hoshino, M. 2013, *PhRvL*, 111, 215003
- Medvedev, M. V., & Loeb, A. 1999, *ApJ*, 526, 697
- Medvedev, M. V. 2006, *ApJL*, 651, L9
- Newman, D. L., Goldman, M. V., Ergun, R. E., & Mangeney, A. 2001, *PhRvL*, 87, 255001
- Niemiec, J., Pohl, M., Stroman, T. & Nishikawa, K.-I. 2008, *ApJ*, 684, 1174
- Niemiec, J., Pohl, M., Bret, A. & Wieland, V. 2012, *ApJ*, 759, 73
- Nishikawa, K.-I., Hardee, P., Richardson, G., Preece, R., Sol, H., & Fishman, G. J. 2003, *ApJ*, 595, 555
- . 2005, *ApJ*, 622, 927
- Nishikawa, K.-I., Niemiec, J., Hardee, P. E., Medvedev, M., Sol, H., Mizuno, Y., Zhang, B., Pohl, M., Oka, M., & Hartmann, D. H. 2009, *ApJL*, 698, L10
- Nishikawa, K. I., Frederiksen, J. T., Nordlund, A., Mizuno, Y., Hardee, P. E., Niemiec, J., Gomez, J. L., Péér, A., Dutan, I., Meli, A., Sol, H., Pohl, M., & Hartman, D. H. 2016, *ApJ*, 820, 94
- Panaitescu, A. 2001, *ApJ*, 556, 1002
- Panaitescu, A., & Kumar, P. 2002, *ApJ*, 571, 779
- Park, J., Workman, J. C., Blackman, E. G., Ren, C., & Siller, R. 2012, *Physics of Plasmas*, 19, 062904
- Park, J., Ren, C., Workman, J. C., & Blackman, E. G. 2013, *ApJ*, 765, 147
- Reynolds, S. R. 2008, *ARA&A*, 46, 89
- Rybicki, G. B. & Lightman, A. P. 1979, *Radiative Processes in Astrophysics*, John Wiley & Sons, Inc, New York, Third edition
- Sironi, L., & Spitkovsky, A. 2011, *ApJ*, 726, 75
- Sironi, L., Spitkovsky, A., & Arons, J. 2013, *ApJ*, 771, 54
- Shapiro, V. D., & Ücer, D. 2003, *Planet. Space Sci.*, 51, 665
- Spitkovsky, A. 2008a, *ApJL*, 673, L39
- . 2008b, *ApJL*, 682, L5-L8
- Stockem, A. N., Bret, A., Fonseca, R. A., & Silva, L. O., 2015, *Plasma Physics and Controlled Fusion*, 58, 014005
- Tautz, R.C., & Lerche, I. 2012, *Physics Reports*, 520, 1
- Uchiyama, Y., Aharonian, F. A., Tanaka, T., Takahashi, T., & Maeda, Y. 2007, *Nature*, 449, 576
- Webb, G. M., Axford, W. I., & Terasawa, T. 1983, *ApJ*, 270, 537
- Weibel, E. S. 1959, *PhRvL*, 2, 83
- Wieland, V., Pohl, M., Niemiec, J., Rafighi, I., & Nishikawa, K.-I. 2016, *ApJ*, 820, 62
- Yee, K.S., 1966. *IEEE Trans. Antennas Propag.* 14, 302
- Zhang, B., & Kobayashi, S., 2005, *ApJ*, 628, 315

## ALL AUTHORS AND AFFILIATIONS

KAZEM ARDANEH<sup>1</sup> AND DONGSHENG CAI,

Department of Computer Science, University of Tsukuba, Tenoudai 1-1-1, Tsukuba science city, Ibaraki 305-8573,

Japan

AND

KEN-ICHI NISHIKAWA.

Department of Physics, University of Alabama in Huntsville, ZP12, Huntsville, AL 35805, USA

<sup>1</sup>kazem.arrdaneh@gmail.com